

Uncertainty Quantification for Hyperspectral Image Denoising Frameworks based on Sliding-Window Low-Rank Matrix Approximation

Jingwei Song, Shaobo Xia, Jun Wang, Dong Chen, *Member, IEEE*

Abstract—Sliding-window low-rank matrix approximation (LRMA) is a technique widely applied in hyperspectral images (HSI) denoising or completion. The uncertainty quantification of the estimated restored HSI, however, has not been addressed before. The lack of uncertainty of the denoised HSI significantly limits applications like multi-source or multi-scale data fusion, data assimilation and product confidence quantification, since these applications require an accurate approach to describe the statistical distributions of the input data. To address this issue, we propose a prior-free closed-form element-wise uncertainty quantification method for the LRMA based HSI restoration. Our closed-form algorithm overcomes the difficulty of the HSI patch mixing problem caused by the sliding-window strategy used in the conventional LRMA process. The proposed approach only requires the uncertainty of the observed HSI and can yield uncertainty in a limited amount of time and with similar time complexity comparing to the LRMA technique. We conduct extensive experiments to validate that the closed-form uncertainty describes the estimation accurately, is robust to at least 10% ratio of random impulse noises, at the cost of 10–20% additional processing time of the LRMA. The experiments indicate that the proposed closed-form uncertainty quantification method is more applicable to be deployed to real-world applications than the baseline Monte Carlo test, considering the Monte Carlo test involves far heavy computational resources.

Index Terms—Low-rank matrix approximation, hyperspectral images, uncertainty quantification.

I. INTRODUCTION

Data uncertainty, which refers to the lack of sureness about the data [1], is an essential factor to be considered when utilizing data and their derived products [2]. With the given data uncertainties, users can determine whether a product is qualified to be involved in their applications, or how to balance the contributions of different sources of data. For example [3], the minimum detectable deformation can be estimated based on the uncertainty measures in point clouds, based on which engineers can make a proper project plane, including sensor

selection and set-up schemes [4]. In multiple data fusion tasks, the label uncertainties of HSI and point clouds are often considered to achieve high fusion accuracy [5].

In theory, uncertainty can be classified as aleatoric uncertainty and epistemic uncertainty [6]. The aleatoric uncertainty is caused by the noise existed in both data collections and processing steps while the epistemic uncertainty is introduced in the observation models and data post-processing steps [1], [2], [4], [7], [8]. In the scenario of absent of ground truth to measure the model performance, the epistemic uncertainty is ignored and the output uncertainty is defined as the aleatoric uncertainty with the propagation of the arbitrary model. Most researches define the probabilistic density function of the noise as a mixture of the normal distribution and the random distribution. Assuming the random noise is significant small, the uncertainty described with the Gaussian distribution. In HSI restoration, symmetric uncertainty based on mutual information is proposed in [9] and applied to hyperspectral images (HSI) classifications. In HSI unmixing, the end member uncertainty for those unmixing methods based on the normal compositional model is defined as a covariance matrix, based on which unmixing errors can be predicted without knowing the ground truth [10]. The description of the uncertainty is presented in different forms. [1] proposes an entropy-based uncertainty measure for the evaluation of the classification results of multi-spectral remote sensing images. The calculated entropy, denoted as the pixel-wise classification uncertainty, is in linear relation of all the classification results. In [11], the uncertainty of 3D point clouds is defined as the measurement repeatability, realized by the median and two percentiles (5% and 95%) related to repeated measurements.

This paper focuses on the uncertainty quantification in the HSI denoising domain. HSI that consists of hundreds or thousands of spectral bands, has been widely used in various applications (e.g. land cover mapping, pollution monitoring, and crop yield estimation), attributing to its rich spectral information beyond the spatial information. In HSI data processing, image denoising is regarded as an important preprocessing step for advanced applications and has been a heavily researched area in past decades [12]. According to [13], the exiting HSI denoising methods can be categorized into three groups: filter-based methods, model optimization-based methods, and deep learning-based methods. Filter-based methods try to remove noise based on various filters. Classical methods in this category are based on nonlocal filters [14]–[17]. The model optimization-based methods can be further

This work was supported in part of National Natural Science Foundation of China under Grant 41971415. (Corresponding author: Dong Chen)

Jingwei Song is with the College of Civil Engineering, Nanjing Forestry University, Nanjing 210037, China, and the Centre for Autonomous Systems, University of Technology, Sydney, P.O. Box 123, Broadway, NSW 2007, Australia. e-mail: (jingwei.song@student.uts.edu.au).

Shaobo Xia is with the Department of Geomatics Engineering, University of Calgary, T2N 1N4, Canada. e-mail: (shaobo.xia@ucalgary.ca).

Jun Wang is with the Institute of Remote Sensing and Digital Earth, Chinese Academy of Sciences, University of Chinese Academy of Sciences, Beijing, China. e-mail: (wangjun@radi.ac.cn).

Dong Chen is with the College of Civil Engineering, Nanjing Forestry University, Nanjing 210037, China. e-mail: (chendong@njfu.edu.cn).

divided into several classes such as total-variation methods [18], sparse representation-based [19], and sliding-window low-rank matrix-based methods [20]. The major advantages of this group of denoising methods are utilizing image priors and considering spatial and spectral features simultaneously. These methods are often combined to achieve better performance [21], [22]. The last group is based on deep learning frameworks and is attracting rising attention in the past three years [23]. In this group, a recent deep learning-based framework is proposed in [13], which removes hybrid noise under a spatial-spectral framework.

HSI denoising based on the sliding-window low-rank matrix approximation (LRMA) framework has become a state-of-the-art technique in the community [20], [24]. These methods belong to the model optimization-based methods, and the idea is exploiting the low-dimensional structure in the high dimensional data space. The LRMA based studies [20], [21], [25] held the prior that the noise-free HSI can be represented by the low-rank matrix. Thus, the HSI denoising can be viewed as a classical sliding-window low-rank matrix recovery problem. A representative HSI denoising framework based on LRMA is described in [20], where clean image, mixed noise, and Gaussian noise were formulated separately in their objective function which was minimized under low-rank constraints. There are many variants of LRMA-based HSI denoising methods presented in the past five years [21], [24], [26]–[28]. For example, [24] proposed an LRMA-based framework that contains a term named total-variation regularization aiming at preserving spatial information. The spatial-spectral structural in HSI denoising is also exploited via replacing sliding-window low-rank matrix analysis by low-rank tensor approximation [28]. In general, LRMA-based HSI denoising methods can be treated as the state-of-the-art framework which has been widely applied in this area.

Despite the progress in LRMA-based HSI denoising, no research pays attention to the uncertainty quantification of the denoised HSI. Several existing works aim at determining the noise of the raw observation [29], [30] while the confidence of the denoised HSI has been overlooked, which is critical in further applications as discussed in the beginning. However, the quantification of uncertainties for the denoised HSI based on LRMA is difficult due to the nonlinear discontinuous functions in LRMA models (e.g., nuclear norm), which hinders the deduction of the closed-form uncertainty propagation formulations. Recently, [31] proposed an optimal uncertainty quantification and inference method for noisy matrix completion. Inspired by this work, we find that it would be possible to obtain quantified uncertainties of outputs from LRMA-based HSI denoising frameworks.

To handle huge data volumes in HSI, a sliding-window strategy is always applied in HSI denoising [20], [24], which means that the denoised element values are obtained by averaging values from several traversed patches. The mixed value from multiple patches poses difficulty in quantifying the uncertainty for the estimations. Unlike the conventional perspective of multiple observations obey the same i.i.d distribution, the multiple sliding windows are inter-connected in various manner based on their ranges. To tackle these

problems, we introduce and improve the method from [32] to quantify the uncertainty of the low-rank based HSI approach. Note that we assume the input HSI is a mixture of Gaussian noise and random noise. Previous researches [16], [21], [30] already prove that the Poisson noise is the main concern in real HSI data and but can be approximated by the additive Gaussian noise. Based on these conclusions, the Gaussian noise with mean and covariance is suitable to build the uncertainty propagation models.

The main contributions of this paper are three-fold,

- 1) To the best of our knowledge, the uncertainty quantification for denoised HSI based on LRMA is presented for the first time in this paper. We provide a closed-form time-efficient uncertainty propagation model to predict the element-wise uncertainty for the denoised HSI without knowing any ground truth.
- 2) To solve the “uncertainty mixing” problem caused by the sliding-window strategy, we deduce a weighted averaged uncertainty formulation, which turns to be effective based on extensive experiments.
- 3) The proposed uncertainty estimation approach is independent of the choice of the LRMA algorithm. It is based on the global minimum assumption of the LRMA solver, thus more accurate solver leads to better uncertainty description.

The rest of this paper is organized as follows. In Section II, the formulation for the uncertainty propagation under a classical LRMA-based HSI denoising framework is described in detail. Section III shows several experiments on both simulated and real HSI data. The discussions on parameter settings and limitations are presented in Section III. Section IV summarizes this paper.

II. METHODOLOGY

A. Revisiting the general HSI restoration process

Fig. 1 demonstrates the routine process of the LMRA based HSI restoration. The HSI is processed with a 3D sliding window to save the computational burden. For each 3D patch within the window, all the bands are vectorized and stacked into the 2D matrix. The permuted 2D matrix goes through the routine LMRA process, and the result is re-permuted to recover the 3D denoised patch. Finally, all the patches are summarized and averaged to build the restored HSI.

The HSI acquired by the sensor is normally modeled as the 3D image composed of Gaussian noise and random noise:

$$\mathbf{W} = \mathbf{W}^* + \mathbf{G} + \mathbf{N}, \quad (1)$$

where $\mathbf{W} \in \mathbb{R}^{M \times N \times P}$ is the image acquired from the hyperspectral sensor with the size $M \times N$ and P channels, $\mathbf{W}^* \in \mathbb{R}^{M \times N \times P}$ is the noise-free image denoted as the ground truth, $\mathbf{G} \in \mathbb{R}^{M \times N \times P}$ is the element-wise, independent and identically distributed (i.i.d) Gaussian noise and $\mathbf{N} \in \mathbb{R}^{M \times N \times P}$ is the random noise (impulse signal). The random noise \mathbf{N} is normally considered as negligible with regard to \mathbf{G} , and the data quality quantification process is inferring the statistical distribution of \mathbf{G} . In practice, the ground truth HSI \mathbf{W}^* is not able to be obtained. Thus, we denote $\hat{\mathbf{W}}$ as the estimated

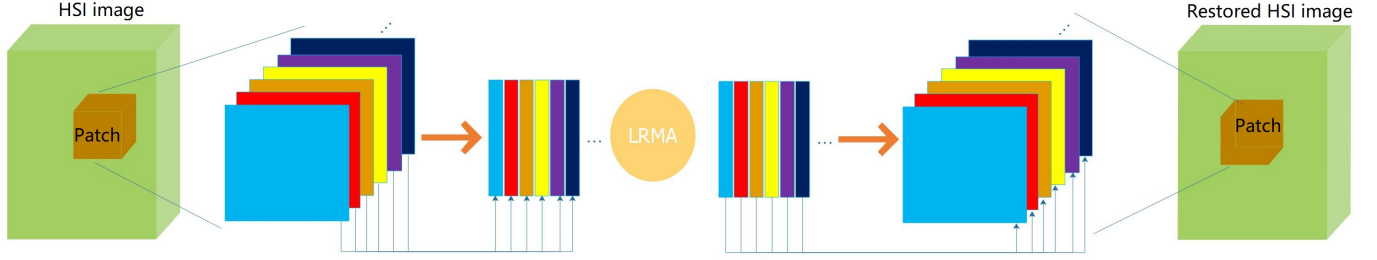


Fig. 1: Illustrated is the routine process of HSI restoration. The 3D matrix on both ends is the raw and denoised HSI. The sliding window goes through the matrix and operates on each patch. For the selected 3D patch matrix, it is converted to a 2D matrix by concatenating each band of the 2D matrix as a 1D vector. The permuted 2D matrix goes through the LRMA process to generate the denoised matrix. Symmetrically, the denoised 2D matrix is inversely permuted to the 3D patch matrix and constitutes the final restored HSI in 3D.

denoised HSI calculated from researches based on the low-rank assumption [21], [22].

The goal of HSI denoising is to recover the denoised $\hat{\mathbf{W}}$ with the 3D HSI noisy observation \mathbf{W} and the exact rank prior. Assuming the random noise \mathbf{N} is negligible, the restored image $\hat{\mathbf{W}}$ is recovered with the following formulation:

$$\begin{aligned} \min_{\hat{\mathbf{W}}} \quad & \mu \text{rank}(\hat{\mathbf{W}}^\#) + \|\mathbf{G}\|_0, \quad \text{s.t. } \hat{\mathbf{W}} = \mathbf{W} + \mathbf{G} \\ \text{such that} \quad & \hat{\mathbf{W}}^\# = g(\hat{\mathbf{W}}) \end{aligned}, \quad (2)$$

where μ is the hyperparameter balancing the two terms. $\text{rank}(\cdot)$ constrains the rank of the input matrix to be no greater than the given rank. $g(\cdot)$ permute the 3D HSI to 2D matrix by vectorizing and concatenate to general 2D matrix (Fig. 1). The low-rank formulation is originally proposed by [33] and named as the ‘‘robust principal component analysis (RPCA)‘‘.

B. The sliding-window in HSI restoration process

HSI restoration differs greatly from the conventional image processing community due to the data size. The extremely large permuted 2D matrix hinders the iterative regular Singular Value Decomposition (SVD) process which is essential in solving Eq. (2). To overcome the heavy computational burden in minimizing the objective function due to the huge HSI size, the HSI is segmented to small patches (denoted as the overlapped sliding window) and solved in parallel. Previous researches view the sliding-window strategy as an engineering trick and ignore the formal mathematical presentation. However, we realize that the special sliding-window structure significantly hinders the uncertainty quantification. The sliding-window version is presented in Eq. (2) by minimizing all patches:

$$\begin{aligned} \min_{\hat{\mathbf{W}}^{(ijk)}} \quad & \mu \text{rank}(\hat{\mathbf{W}}^\#^{(ijk)}) + \frac{1}{2} \|\mathbf{W}^{(ijk)} - \hat{\mathbf{W}}^{(ijk)}\|_F^2 \\ \text{such that} \quad & \hat{\mathbf{W}}^\#^{(ijk)} = g(\hat{\mathbf{W}}^{(ijk)}) \\ & (i, j, k) \in \Omega \end{aligned}, \quad (3)$$

where the matrices $\mathbf{W}^{(ijk)}$, $\hat{\mathbf{W}}^{(ijk)}$ and $\hat{\mathbf{W}}^\#^{(ijk)} \in \mathbb{R}^{J \times J}$ are the patch indexed in (ijk) with regard to \mathbf{W} , $\hat{\mathbf{W}}$ and $\hat{\mathbf{W}}^\#$. J is the

size of the permuted matrix. $\Omega \subseteq \{1, \dots, M'\} \times \{1, \dots, N'\} \times \{1, \dots, P'\}$ is the number of patches regarding to the size of HSI. $\|\cdot\|_F$ is the Frobenius norm minimizing the divergence of the restored HSI patch $\hat{\mathbf{W}}^{(ijk)}$ and the observation $\mathbf{W}^{(ijk)}$. After all the patches are optimized, the optimal $\hat{\mathbf{W}}$ is restored by averaging the overlapped patches $\hat{\mathbf{W}}^{(ijk)}$ element-wisely. By ignoring the random noise, we have the observation corrupted with the element-wise Gaussian noise:

$$\mathbf{W}^{(ijk)} \approx \mathbf{W}^*(ijk) + \mathbf{G}^{(ijk)}, \quad \mathbf{G}^{(ijk)} \stackrel{\text{i.i.d.}}{\sim} \mathcal{N}(0, \sigma_0^2), \quad (4)$$

where σ_0^2 is the variance of the noise obtained from image or estimated by algorithms like [25], the Gaussian noise $\mathbf{G}^{(ijk)}$ is the Gaussian noise at patch (ijk) . In previous studies, the choice of rank is often estimated by manual-tuning strategies based on the differences between the reconstructed signal and the original one [21].

The idea of Eq. (3) is to convert the 3D patch into a typical 2D small-size matrix so that the conventional low-rank factorization algorithm can handle with the limited computational resources. It is often solved with Lagrange multiplier or augmented Lagrange multiplier (ALM) and there are off-the-shelf low-rank solvers. In this work, we choose the GoDec algorithm proposed by [34] to be consistent with the LRMA method [20]. But we would like to address that the proposed uncertainty quantification method is independent of the solver since it only assumes the estimation of LRMA is close to the global minimum. The better performance of the LRMA solver, the more accurate confidence interval our method describes.

After all small overlapped patches go through the process of Eq. (3), the optimized denoised patches are summed up to restore the HSI:

$$\hat{\mathbf{W}} = \left[\sum_{i,j,k \in \Omega} f_p(\hat{\mathbf{W}}^{(ijk)}) \right] \oslash \mathbf{Q}, \quad (5)$$

where $f_p(\cdot)$ is the padding function to convert the patch to the same size of $\hat{\mathbf{W}}$ by padding the rest elements with 0. The matrix $\mathbf{Q} \in \mathbb{R}^{M \times N \times P}$ counts the number of the patches valid on each voxel. \oslash is the Hadamard division operator.

C. The general framework

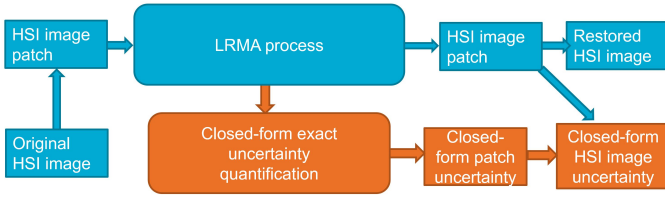


Fig. 2: The general framework of the proposed approach. Blue is the typical LRMA process ([20] as an example). Our work aims at providing an extra module to quantify the uncertainty of the output, the restored HSI, using the LRMA algorithm.

Fig. 2 demonstrates the general framework as well as the relationship with the routine LRMA approaches. In the LRMA process, the temporary variable, 2D sliding-window patch, is utilized to provide the uncertainty to the HSI patch based on our closed-form formulation. After the HSI patch and its associated closed-form uncertainty are generated, the routine LRMA approach averages them to yield the restored HSI, and we correspondingly provide a closed-form uncertainty propagation to quantify the final restored HSI. As demonstrated in Fig. 2, through all the processes, the proposed approach is independent of the choice of the low-rank solver. It can also be easily integrated into the derivations of the LRMA process. On top of this, since our method is a closed-form solution and only utilize the temporary variables, the processing time is small regarding the routine LRMA process.

One major contribution of this work is that it provides an element-wise closed-form solution to quantify the uncertainty in a time-efficient manner. For the restored HSI $\hat{\mathbf{W}}$, one straight forward way of element-wise uncertainty quantification is conducting the Monte Carlo test with the given statistical distribution of the observation \mathbf{W} . However, the size of HSI is notoriously large, and it poses a heavy computational burden to conduct a massive amount of Monte Carlo test. Rough one-time process in [20] on $100 \times 100 \times 100$ HSI takes 20 minutes with a typical commercial desktop. While a convincing uncertainty quantification requires a reasonable number of trials, the Monte Carlo test is inefficient to be applied to the element-wise HSI uncertainty quantification.

Another benefit of this research is that it solves the uncertainty propagation for the sliding-window process. The uniqueness of the HSI is that the permuted 2D matrix after the dimension reduction procedure is huge. The solution cannot be achieved with a one-time LRMA process. Instead, researchers adopt the sliding-window strategy to segment the HSI into many small patches and process them in parallel. The different statistical properties of each overlapped patches gain difficulty in quantifying the uncertainty of the final restored HSI. We also solve this problem and present a closed-form solution for sliding-window element-wise closed-form HSI uncertainty quantification.

D. Uncertainty quantification for the exact low-rank factorization

This section focuses on solving the uncertainty quantification for the patch-wise low-rank factorization process (Eq. (3)), and HSI patch-based averaging (Eq. (5)) will be discussed in next section. Recent research [31] proposes an uncertainty quantification method for the exact low-rank 2D matrix. This element-wise algorithm can quantify the confidence for a common low-rank based 2D matrix denoising algorithm. Synthetic and real-world tests validate the efficiency of this method. We introduce this approach and modify it to enable the quantification of the uncertainty of each estimated 3D HSI patch $\hat{\mathbf{W}}^{(ijk)}$ from Eq. (3).

In the patch optimization process shown in Eq. (3), we first aim to quantify the uncertainty of the temporary 2D square matrix $\hat{\mathbf{W}}^{\#(ijk)}$ ($\hat{\mathbf{W}}^{\#(ijk)} = g(\hat{\mathbf{W}}^{(ijk)})$) and it can be any patch in Ω . We denote the ground truth of $\hat{\mathbf{W}}^{\#(ijk)}$ and $\hat{\mathbf{W}}^{(ijk)}$ as $\mathbf{W}^{\#(ijk)}$ and $\mathbf{W}^{(ijk)}$. For the sake of conciseness, the rank- r SVD decomposition is $\mathbf{W}^{\#(ijk)} = \mathbf{U}^{*(ijk)} \Sigma^{*(ijk)} \mathbf{V}^{*(ijk)\top}$. For conciseness, we simplify $(\mathbf{U}^{*(ijk)}, \Sigma^{*(ijk)}, \mathbf{V}^{*(ijk)})$ by ignoring the patch index (ijk) and rewrite as $(\mathbf{U}^*, \Sigma^*, \mathbf{V}^*)$. Two matrices are defined as the product of the unitary matrix and the squared singular matrix: $\mathbf{X}^* \triangleq \mathbf{U}^* \Sigma^{*1/2} \in \mathbb{R}^{K \times r}$, $\mathbf{Y}^* \triangleq \mathbf{V}^* \Sigma^{*1/2} \in \mathbb{R}^{L \times r}$. The following rules apply:

$$\mathbf{X}^{*\top} \mathbf{X}^* = \mathbf{Y}^{*\top} \mathbf{Y}^* = \Sigma^*. \quad (6)$$

Following the above definition, the ground truth 2D temporary matrix $\mathbf{W}^{\#(ijk)} = \mathbf{X}^* \mathbf{Y}^{*\top}$. Similarly, we define the estimated version $\hat{\mathbf{W}}^{\#(ijk)} \approx \hat{\mathbf{X}} \hat{\mathbf{Y}}^\top$ where $\hat{\mathbf{X}}$ and $\hat{\mathbf{Y}}$ are the estimated matrices regarding to \mathbf{X}^* and \mathbf{Y}^* . We also have the estimated version of Σ^* as $\hat{\Sigma}$:

$$\hat{\Sigma} = \hat{\mathbf{X}}^\top \hat{\mathbf{X}} = \hat{\mathbf{Y}}^\top \hat{\mathbf{Y}} \approx \Sigma^*. \quad (7)$$

Theorem 1. For the estimations of the auxiliary matrices $\hat{\mathbf{X}}$ and $\hat{\mathbf{Y}}$, the difference to the rectified ground truth $\hat{\mathbf{X}}$ and $\hat{\mathbf{Y}}$ are:

$$\begin{aligned} \hat{\mathbf{X}} \hat{\mathbf{R}} - \mathbf{X}^* &= \mathbf{Z}_X + \Psi_X \\ \hat{\mathbf{Y}} \hat{\mathbf{R}} - \mathbf{Y}^* &= \mathbf{Z}_Y + \Psi_Y \end{aligned}, \quad (8)$$

where unitary matrix $\hat{\mathbf{R}} \in \mathbb{R}^{r \times r}$ ($\hat{\mathbf{R}} \hat{\mathbf{R}}^\top = \mathbf{I}$ and \mathbf{I} is identical matrix) is the rectification matrix to rectify $(\hat{\mathbf{X}}, \hat{\mathbf{Y}})$ to $(\mathbf{X}^*, \mathbf{Y}^*)$. The rows of the error matrix $\mathbf{Z}_X \in \mathbb{R}^{K \times r}$ (resp. $\mathbf{Z}_Y \in \mathbb{R}^{L \times r}$) are independent and obeys:

$$\begin{aligned} \mathbf{Z}_X^\top \mathbf{e}_v &\stackrel{\text{i.i.d.}}{\sim} \mathcal{N}(0, \sigma_0^2 (\Sigma^*)^{-1}), & \text{for } 1 \leq v \leq K \\ \mathbf{Z}_Y^\top \mathbf{e}_v &\stackrel{\text{i.i.d.}}{\sim} \mathcal{N}(0, \sigma_0^2 (\Sigma^*)^{-1}), & \text{for } 1 \leq v \leq L \end{aligned}, \quad (9)$$

where \mathbf{e}_v is the basis vector and $\Psi_X \in \mathbb{R}^{K \times r}$, $\Psi_Y \in \mathbb{R}^{L \times r}$ are the residual matrices. We provide the proof in Section A.

The residual noises Ψ_X and Ψ_Y are negligible comparing to \mathbf{Z}_X and \mathbf{Z}_Y and Eq. (8) is approximated to:

$$\begin{aligned} \hat{\mathbf{X}} \hat{\mathbf{R}} - \mathbf{X}^* &\approx \mathbf{Z}_X \\ \hat{\mathbf{Y}} \hat{\mathbf{R}} - \mathbf{Y}^* &\approx \mathbf{Z}_Y \end{aligned}. \quad (10)$$

Assuming that the first-order expansion is reasonably tight and omitting the , the element-wise error between the estimation $\hat{\mathbf{W}}_{uv}^{\#(ijk)}$ and the ground truth $\mathbf{W}_{uv}^{\#(ijk)}$ at the position uv is:

$$\begin{aligned}
& \hat{\mathbf{W}}_{uv}^{\#(ijk)} - \mathbf{W}_{uv}^{\#*(ijk)} \\
&= [\mathbf{e}_u^\top \hat{\mathbf{X}}\hat{\mathbf{R}}(\hat{\mathbf{Y}}\hat{\mathbf{R}})^\top \mathbf{e}_v - \mathbf{e}_u^\top (\mathbf{X}^*\mathbf{Y}^{*\top}) \mathbf{e}_v] \\
&= [\mathbf{e}_u^\top (\hat{\mathbf{X}}\hat{\mathbf{R}} - \mathbf{X}^* + \mathbf{X}^*)(\hat{\mathbf{Y}}\hat{\mathbf{R}} - \mathbf{Y}^* + \mathbf{Y}^*)^\top \mathbf{e}_v - \mathbf{e}_u^\top (\mathbf{X}^*\mathbf{Y}^{*\top}) \mathbf{e}_v] \\
&\approx [\mathbf{e}_u^\top (\hat{\mathbf{X}}\hat{\mathbf{R}} - \mathbf{X}^*)\mathbf{Y}^{*\top} \mathbf{e}_v + \mathbf{e}_u^\top \mathbf{X}^*(\hat{\mathbf{Y}}\hat{\mathbf{R}} - \mathbf{Y}^*)^\top \mathbf{e}_v] \\
&= [\mathbf{e}_u^\top (\mathbf{Z}_X \mathbf{Y}^{*\top}) \mathbf{e}_v + \mathbf{e}_u^\top (\mathbf{X}^* \mathbf{Z}_Y^\top) \mathbf{e}_v],
\end{aligned} \tag{11}$$

where the bases \mathbf{e}_u , \mathbf{e}_v localize the elements involved in calculating element in position (u, v) . After some manipulation, we have the element-wise variance of the error as:

$$\begin{aligned}
& \text{var}(\hat{\mathbf{W}}_{uv}^{\#(ijk)} - \mathbf{W}_{uv}^{\#*(ijk)}) \\
&\stackrel{(i)}{\approx} [\text{var}(\mathbf{e}_u^\top (\mathbf{Z}_X \mathbf{Y}^{*\top}) \mathbf{e}_v) + \text{var}(\mathbf{e}_u^\top (\mathbf{X}^* \mathbf{Z}_Y^\top) \mathbf{e}_v)] \\
&\stackrel{(ii)}{=} \sigma_0^2 [\mathbf{e}_v^\top \mathbf{Y}^* (\Sigma^*)^{-1} \mathbf{Y}^{*\top} \mathbf{e}_v + \mathbf{e}_u^\top \mathbf{X}^* (\Sigma^*)^{-1} \mathbf{X}^{*\top} \mathbf{e}_u] \\
&\stackrel{(iii)}{=} \sigma_0^2 (\|\mathbf{U}_{u,\cdot}^*\|_2^2 + \|\mathbf{V}_{v,\cdot}^*\|_2^2) = \sigma_0^2 v_{uv}^*,
\end{aligned} \tag{12}$$

where (i) is from the **theorem 1** since \mathbf{Z}_X and \mathbf{Z}_Y are nearly independent. (ii) is from the Eq. (8). (iii) $\mathbf{U}_{u,\cdot}^*$ and $\mathbf{V}_{v,\cdot}^*$ are the u/v th row of \mathbf{U}^* and \mathbf{V}^* . For conciseness, we define $v_{uv}^* = (\|\mathbf{U}_{u,\cdot}^*\|_2^2 + \|\mathbf{V}_{v,\cdot}^*\|_2^2)$. $\text{var}(\cdot)$ is the variance of the input.

In practice, the rows of the ground truth $\mathbf{U}_{u,\cdot}^*$ and $\mathbf{V}_{v,\cdot}^*$ are impossible to obtain. Assuming the solver achieves solution closing to the global minimum, we approximate them with the estimated version $\hat{\mathbf{U}}_{u,\cdot}$ and $\hat{\mathbf{V}}_{v,\cdot}$, which are the u/v th row of the estimations $\hat{\mathbf{U}}$ and $\hat{\mathbf{V}}$. Thus the element-wise variance can be approximated as:

$$\text{var}(\hat{\mathbf{W}}_{uv}^{\#(ijk)} - \mathbf{W}_{uv}^{\#*(ijk)}) \approx \sigma_0^2 (\|\hat{\mathbf{U}}_{u,\cdot}\|_2^2 + \|\hat{\mathbf{V}}_{v,\cdot}\|_2^2) = \sigma_0^2 \hat{v}_{uv}, \tag{13}$$

where \hat{v}_{uv} can be regarded as the estimated version of v_{uv}^* . Considering the relationship of $\mathbf{W}_{uv}^{\#*(ijk)}$ and $\hat{\mathbf{W}}_{uv}^{\#(ijk)}$, the corresponding variance of $\hat{\mathbf{W}}_{uv}^{\#(ijk)}$ is Eq. (14) and provides a closed-form variance describing the confidence of $\hat{\mathbf{W}}_{uv}^{\#(ijk)}$. The variance of $\hat{\mathbf{W}}_{uv}^{\#(ijk)}$ is:

$$\sigma_\xi^{(ijk)^2} = \text{var}(\hat{\mathbf{W}}_{uv}^{\#(ijk)} - \mathbf{W}_{uv}^{\#*(ijk)}) \approx g^{-1}(\sigma_0^2 \hat{v}_{uv}), \tag{14}$$

where $g^{-1}(\cdot)$ is the inverse permutation function of $g(\cdot)$. $\xi \subseteq \{1, \dots, M\} \times \{1, \dots, N\} \times \{1, \dots, P\}$ is the corresponding 3D index of the 2D uv at patch (ijk) .

E. Uncertainty estimation for sliding-window

Another unique character in uncertainty quantification in the LRMA technique is the ‘‘uncertainty mixing’’ caused by the sliding-window strategy. Unlike averaging all patches to generate the final restored HSI (Eq. (2)), the uncertainty of the product does not follow the typical error propagation like estimating uncertainty for multiple observations [35]. In the scenario of uncertainty estimation for i.i.d observation, if the variance of each observation is σ_o^2 and we conduct n times observation, the variance of the averaged observation is $\frac{1}{n}\sigma_o^2$. This shows that the accuracy of the averaged observation is n times accurate than every single observation. But in the LRMA process, we only observe once. If we can process the whole

HSI in one-time LRMA and the accuracy is σ_o^2 , the sliding-window strategy in LRMA should not exceeds σ_o^2 because no new information is introduced. In other words, $\frac{1}{n}\sigma_o^2$ is not the correct uncertainty. The difference between the multiple i.i.d observations and single processing scenarios are that the former holds i.i.d for all the events while the observations in latter are mutually co-related. In other words, the covariance between the overlapped patches in LRMA is not null. For two related events X and Y , the ratio η is often defined to describe the relationship:

$$\eta = \frac{\text{cov}(X, Y)}{\sqrt{\text{var}(X) \cdot \text{var}(Y)}}, \tag{15}$$

where $\text{cov}(\cdot)$ defines the covariance of the two events. If η is 0, it means the events X and Y are i.i.d. If η is 1, it indicates the events X and Y are linearly correlated, and they are in the highest correlation.

We provide a toy example as the weighted average of event X and Y as $F = aX + bY$. Assuming the variance of X and Y are σ_X^2 and σ_Y^2 , the propagated uncertainty of F is σ_F^2 :

$$\sigma_F^2 = a^2 \sigma_X^2 + b^2 \sigma_Y^2 + 2\eta_{XY} ab \sigma_X \sigma_Y, \tag{16}$$

where η_{XY} is the variance ratio defining the relation between events X and Y .

For convenience, we rewrite Eq. (5) to the element-wise form:

$$\hat{\mathbf{W}}_\xi = \frac{1}{\phi(\xi)} \sum_{(i,j,k) \in \Phi(\xi)} f_p(\hat{\mathbf{W}}^{(ijk)})_{uv} \tag{17}$$

such that $(u, v) = G(\xi)$,

where $\Phi(\xi)$ defines the index of the patches covering the position (u, v) and $\phi(\xi)$ is the number of those patches. Similar to the permutation function $g(\cdot)$, $G(\cdot)$ is converting the 3D index of $\hat{\mathbf{W}}$ to the 2D permuted version $\hat{\mathbf{W}}^\#$. Denoting the element-wise variance for each $f_p(\hat{\mathbf{W}}^{(ijk)})_{uv}$ is $\sigma_{uv}^{(ijk)}$, based on the uncertainty propagation theory, we achieve the variance describing $\hat{\mathbf{W}}_{uv}$ as:

$$\begin{aligned}
\hat{\sigma}_\xi^2 &= \frac{1}{\phi(\xi)^2} \sum_{(i,j,k) \in \phi(\xi)} \sigma_\xi^{(ijk)^2} + \\
&\frac{1}{\phi(\xi)^2} \sum_{(i,j,k) \in \phi(\xi)} \sum_{(i',j',k') \in \phi(\xi)} 2\eta^{(ijk)(i'j'k')} \sigma_\xi^{(ijk)} \sigma_\xi^{(i'j'k')},
\end{aligned} \tag{18}$$

where each (i, j, k) is different from (i', j', k') . $\eta^{(ijk)(i'j'k')}$ defines the relation between the element ξ at patch (ijk) and patch $(i'j'k')$. Readers may aware that this is an extended multiple events version of the toy example Eq. (16).

We provide a practical solution to estimate the optimal ratio $\eta^{(ijk)(i'j'k')}$. Suppose the adopted low-rank solver (GoDec algorithm in this paper) achieves the global minimum and the information in each patch is fully exploited, the information for the denoised element ξ in the patch $\hat{\mathbf{W}}^{(ijk)}$ is determined by the information embedded of all the elements within the patch $\hat{\mathbf{W}}^{(ijk)}$. Obviously, the mutual information encoded in two overlapping patches is linearly related to the number of elements shared by the overlapping patches [36]. Thus the

mutual information of the element from two patches is linearly related to the number of shared elements within two patches. Therefore, the optimal ratio between two patches $\eta^{(ijk)(i'j'k')}$ is closing to:

$$\eta^{(ijk)(i'j'k')} \rightarrow \left[\frac{N((ijk), (i'j'k'))}{KL} \right]^{-}, \quad (19)$$

where $N((ijk), (i'j'k'))$ defines the number of shared elements within patch (ijk) and patch $(i'j'k')$. The ratio on the left is closing but smaller to the right. Fig. 3 presents an example the Eq. (19). Each neighboring block pairs hold 50% overlap. Based on the static of number of overlapping elements, the η of the pairs (1,2), (2,3), (3,4) and (4,1) are 0.5 while the η of pairs (1,3) and (2,4) is 0.25.

We should also emphasize that Eq. (19) of $\eta^{(ijk)(i'j'k')}$ is an ideal case that assumes the low-rank solver achieves the global minimum solution; in normal cases, the real $\eta^{(ijk)(i'j'k')}$ should be smaller because the information is not fully exploited making the mutual information and number of elements not strictly linearly related. All other things being equal, a smaller ratio will lead to a smaller variance and thus slightly over-confidence.

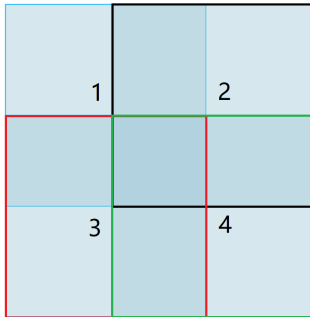


Fig. 3: An example explaining the definition of mutual information defined in Eq. (19). Each of the four 2D overlapped patch 1, 2, 3 and 4 has four pixels.

F. The impact of random noise

The conclusion of Eq. (14) is based on the assumption that the noises $\Psi_{\mathbf{X}}$ and $\Psi_{\mathbf{Y}}$ are significantly smaller than the variables $\mathbf{Z}_{\mathbf{X}}$ and $\mathbf{Z}_{\mathbf{Y}}$ with the normal distribution. If the $\Psi_{\mathbf{X}}$ and $\Psi_{\mathbf{Y}}$ are not ignored, the conclusion does not hold. Therefore, it remains difficult to quantify the impact of the random noise against the Gaussian noise. However, as [33] points out, the RPCA like formulation (Eq. (3).) is robust against the random noise since the low-rank solver will adjust uses the norm-1 or norm-2 to regularize the state matrix. Correspondingly, elements not corrupted by the random noise is unaffected while the impulse noise can be identified. Therefore, regarding the impact of random noise, the robustness of our approach is closely related to the choice of the LRMA algorithm. It should be noted that most existing HSI denoising studies focus on modeling Gaussian noise [21], [25]. A few LRMA-based methods address the non-Gaussian noise [24]. These approaches utilize a total-variance related term to filter out

TABLE I: The coverage rates of $\text{var}(\hat{\mathbf{W}}_{\xi}^{(l)} - \overline{\mathbf{W}}_{\xi})$ for different σ_0 over 100 Monte Carlo trials. ‘‘Std’’ denotes the standard deviation. The proposed closed-form uncertainty estimation approach describes the probability distribution well.

σ_0	Indian		University of Pavia		Washington, D.C	
	Mean	Std	Mean	Std	Mean	Std
0.075	0.9579	0.0371	0.9476	0.0292	0.9368	0.0348
0.050	0.9576	0.0383	0.9556	0.0263	0.9501	0.0311
0.100	0.9643	0.0319	0.9652	0.0233	0.9626	0.0266
0.125	0.9704	0.0273	0.9735	0.0205	0.9712	0.0297

non-Gaussian noise in HSI, aiming at keeping good boundaries after filtering. Similarly, the uncertainty estimated from this research is also capable to be integrated with [24], as the total-variance term is just a constraint.

III. RESULTS AND DISCUSSION

We validate the proposed method on the Indian Pines dataset (simulation dataset)¹, University of Pavia datasets (real dataset)² and Washington, D.C mall dataset³ (real dataset). The Indian Pines dataset is the subset of the data gathered by the AVIRIS sensor. It consists of 145×145 pixels and 224 spectral reflectance bands in the wavelength range of $0.42.510^{-6}$ meters and covers the Indian Pines test site in North-western region, Indiana. The Indian Pines scene contains two-thirds agriculture, and one-third forest or other natural perennial vegetation. We adopt the ground truth of the Indian Pines dataset and simulate with arbitrary Gaussian noise. The University of Pavia dataset is acquired by the ROSIS sensor covering the Pavia, northern Italy. It consists of 610×610 pixels with 103 spectral bands, but some of the samples in the images contain no information and have to be discarded before the analysis. The geometric resolution is 1.3 meters. We select a subset of $610 \times 610 \times 103$ in the experiments. In the Washington, D.C mall dataset, the whole image contains 191 spectral bands with a size of 1208×307 . We clip the image with the size $256 \times 256 \times 191$ in our experiment. Fig. 4 shows the false-color image of the three datasets.

To provide convincing validations, we strictly follow the parameter and noise setting of the selected LRMA method [20]. The size of the sliding window is $20 \times 20 \times P$ where P are the number of bands of the dataset. The step size is 4 and the rank r is set to 7. In the image restoration process, all images are normalized to the range $[0 \ 1]$. The zero-mean Gaussian noise is uniformly imposed on all pixels of the datasets with different levels of noise. Considering the two real datasets do not have ground truth, we adopt the output of [20] as the ground truth. The impact of impulse noise is further tested on the datasets. We would like to address that this research is based on the known raw HSI noise, which can be retrieved following previous methods [29], [30].

¹<https://engineering.purdue.edu/biehl/MultiSpec/hyperspectral.html>

²http://www.ehu.es/ccwintco/index.php?title=Hyperspectral_Remote_Sensing_Scenes

³<https://engineering.purdue.edu/biehl/MultiSpec/hyperspectral.html>

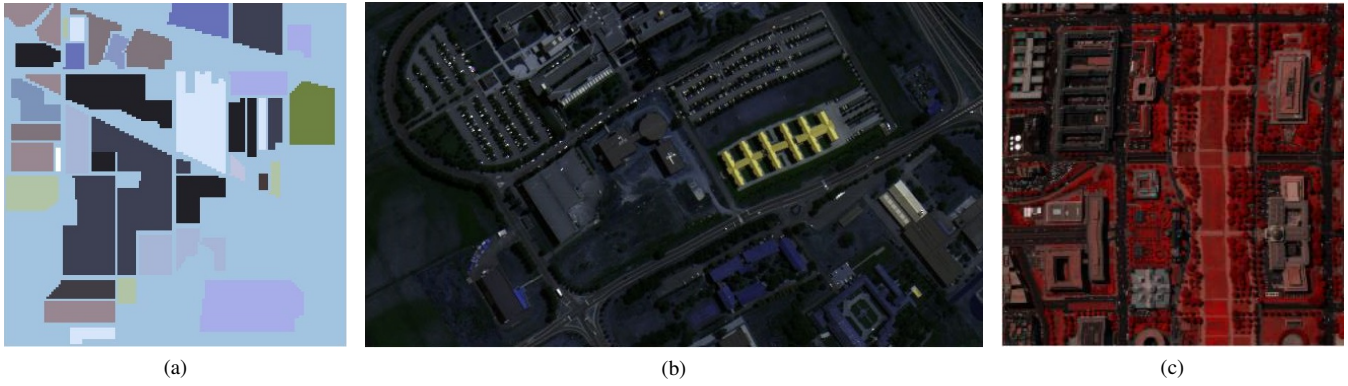


Fig. 4: (a) is the false-color image of the Indian dataset with bands composed of the bands 10, 37 and 70. This is the manually classified ground truth of the Indian dataset. (b) is the false-color image of the University of Pavia dataset composed of the bands 20, 42, and 72. (c) is the false-color image of the Washington D.C. dataset composed of bands 60, 27 and 17.

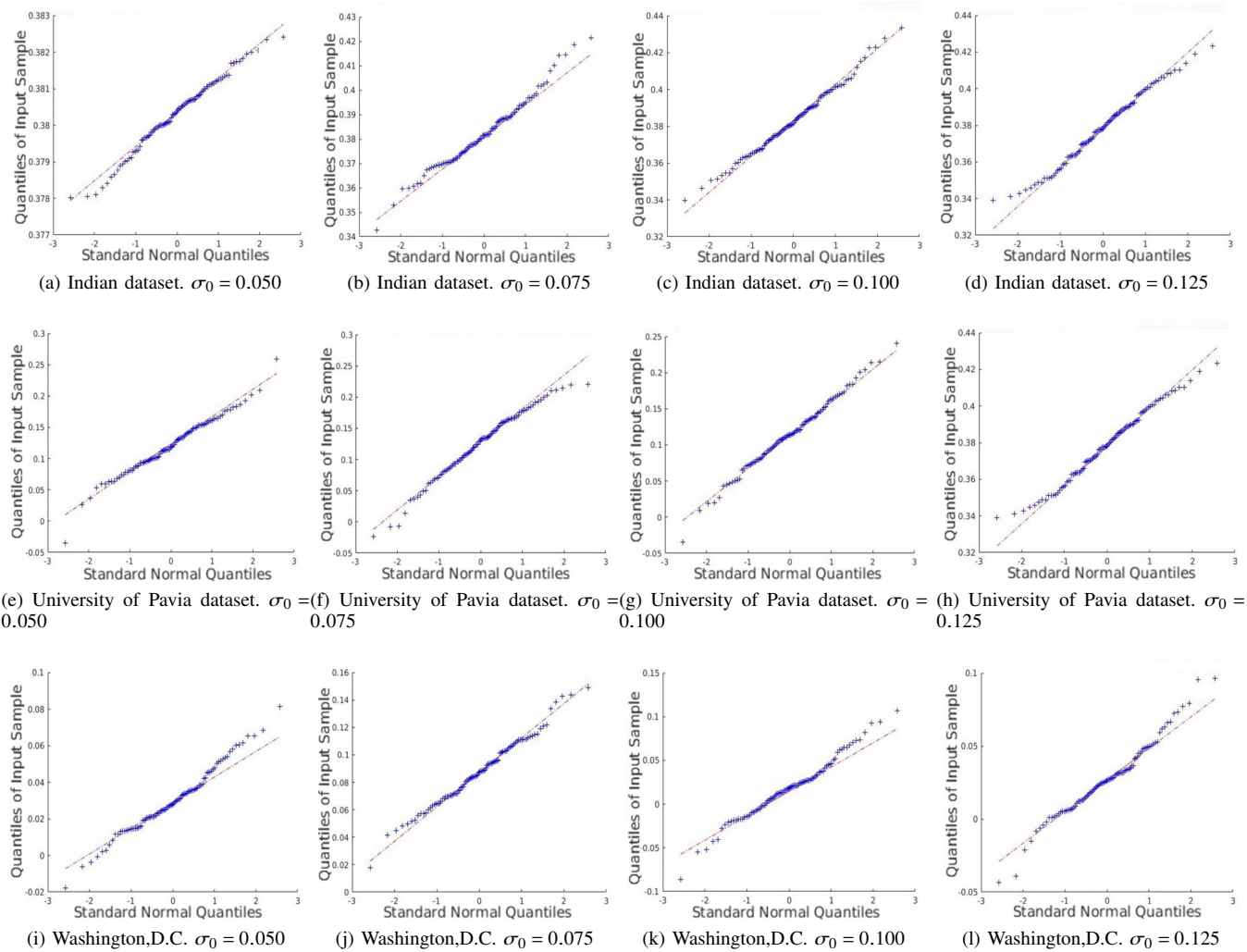


Fig. 5: Illustrated are the (Q-Q) plots of a random element position over 100 independent trials for noise in the three datasets.

A. The validation of the accurate uncertainty description

The accuracy of the proposed closed-form uncertainty quantification method is extensively validated with numerical Monte Carlo tests. We impose different levels of Gaussian

noises on the HSI. Numerical experiments provide enough samples to test if the statistical distributions of the samples are described accurately with the output confidence interval. Specifically, $T = 100$ times of Monte Carlo tests are performed

TABLE II: The probability values (p -value) of the Shapiro-Wilk test of datasets Indian, University of Pavia and Washington, D.C mall. We cite the corresponding element positions of Fig. (5) as an example through all the tests. The p -value > 0.05 indicates a significant possibility that the element is normally distributed.

Dataset	Indian	University of Pavia	Washington, D.C
0.050	0.4239	0.1531	0.2046
0.075	0.1103	0.1924	0.0585
0.100	0.8498	0.7537	0.6977
0.125	0.4346	0.1531	0.5331

on the input of the same noise σ_0^2 . For each element of the estimated HSI in trial l at position ξ as $\hat{\mathbf{W}}_\xi^{(l)}$, we define its deviation to the corresponding T times mean value as $\bar{\mathbf{W}}_\xi$. The deviation to the mean is defined as:

$$e_\xi^{(l)} = \|\hat{\mathbf{W}}_\xi^{(l)} - \bar{\mathbf{W}}_\xi\|_1, l \in [1, \dots, T]. \quad (20)$$

If the closed-form solution describes statistical distribution of the estimation well, 95% of $\hat{\mathbf{W}}_\xi^{(l)}$ should fall within the range of $[\bar{\mathbf{W}}_\xi - 1.96\hat{\sigma}_\xi, \bar{\mathbf{W}}_\xi + 1.96\hat{\sigma}_\xi]$. Following Eq. (20), we define the the ratio of $e_\xi^{(l)}$ falls within the $1.96\hat{\sigma}_\xi$ bound as the element-wise **coverage rate**. The average of all elements' **coverage rate** is the **average coverage rate**. Table I presents the average and standard deviation of the coverage rate. It indicates that the uncertainty robustly and accurately describes the element-wise denoised HSI. Most of the average coverage rates are a bit higher than 95% meaning the algorithm is over-confident. This supports our claim of smaller ratio (Eq. (19)) and over-confidence of the uncertainty mixing.

B. The validation of the normal distribution of the restored HSI

On top of the **average coverage rate**, we also adopt the Monte Carlo experiments to prove that the restored HSI $\hat{\mathbf{W}}^{(l)}$ has innate Gaussian distribution. Quantile-Quantile (Q-Q) plots and Shapiro-Wilk tests are conducted to validate our claim. Fig. 5 demonstrates the (Q-Q) plots of all the datasets. Note that we randomly plot one element of each dataset as an example, but all other elements are similar since the observation is isotropic. Fig. 5 indicates that the Monte Carlo estimation of all the trials $\hat{\mathbf{W}}^{(l)}$ is close to a line, thus the sample follows the Gaussian distribution.

In the Shapiro-Wilk tests, since it is not possible to present all the elements, we randomly choose several elements over the three datasets with different levels of Gaussian noise. The results are presented in Table II. The p -value indicates that all samples follow the normal distribution well (> 0.05). Since all pixel are imaged on the same condition and their statistics should be consistent (either obey or reject the normal distribution assumption), we can conclude that the restored HSI still follows the normal distribution.

C. Time consumption comparison

In addition to the accuracy tests, we further validate that the closed-form uncertainty estimation method has similar

TABLE III: The time consumption comparisons of the Monte Carlo uncertainty estimation, the LRMA method [20] and our method. Note that in the Monte Carlo tests, we run 100 trials. The time is recorded in second.

Dataset	Monte Carlo	LRMA	Monte Carlo+Uncertainty
Indian	7862	653	864
University of Pavia	8393	815	930
Washington, D.C	12437	1023	1590

time consumption as the LRMA, and far less than the Monte Carlo numerical tests. We adopt the LRMA code directly from [20] and add the uncertainty estimation module. The proposed algorithm, the LRMA, and Monte Carlo tests are all implemented with Matlab 2019a. In the Monte Carlo tests, we adopt the Parallel Computing Toolbox of Matlab to fasten the steps. The hardware set is $2 \times 3.1GHz$ Intel Xeon E5-2687wv3 and 64 GB DDR4-Ram. In the Monte Carlo experiments, all 20 CPU threads are fully utilized. Note that in Monte Carlo tests, each element is covered by several sliding windows and the memory is not enough to store all sliding window, we first calculate the result of the patch, store it on the hard disk and reload to calculate each element in the final step.

Table III shows the time consumption of the Monte Carlo uncertainty estimation, the LRMA method [20] and our method integrated into [20]. It indicates our closed-form estimation does not add a heavy burden to the LRMA method while the Monte Carlo test involves massive amounts to time. As indicated by Eq. (12), the proposed approach only requires no more than one band-wise SVD decomposition of the given HSI in addition to original LRMR solver.

D. The impact of random noise

In addition to the coverage rate tests, we further validate that the proposed approach is robust to the random noise from the sensor. As the Eq. (2) shows, our work ignores the random noise \mathbf{N} and only assumes the residual follows the Gaussian noise \mathbf{G} . We also claim in Section II-F that the proposed method is robust to the random pollution like impulse noise, dead lines and stripes [37], [38]. We conduct the tests by deliberately corrupting the original HSI with random noise and test the performance of the proposed uncertainty quantification method. We simulate different ratios of pulse noises on the all the datasets and present the coverage rate of the Monte Carlo experiments.

Table IV shows the Monte Carlo experiments on different coverage rate. The table indicates relations of the robustness of the proposed closed-form method and the coverage rate. It shows that when the noise σ_0 is greater than 0.1, the uncertainty quantification approach is less sensitive to the random pulse noises. When the noise σ_0 is less than 0.075, the proposed method is susceptible to random noise. Theoretically, the proposed approach is only effective to the Gaussian noise as indicated on the prior of the derivation Eq. (2). Therefore, smaller Gaussian noise means less reliable of the assumption that \mathbf{N} is less than \mathbf{G} in Eq. (1). Thus, the results from the closed-form approach are less reliable. As the indicates that When the Gaussian noise of the observation is small, the

TABLE IV: The coverage rate and related standard deviation over different ratios of salt-and-pepper random noise. We exert $m\%$, $m \in [5, 10, 20, 30]$ ratios of salt-and-pepper random noise over the observations., and test the coverage rates of in different scenarios over 100 Monte Carlo trials.

Dataset	σ_0	5%		10%		20%		30%	
		Mean	Std	Mean	Std	Mean	Std	Mean	Std
Indian	0.050	0.9006	0.0619	0.8429	0.0770	0.7309	0.0924	0.6278	0.0952
	0.075	0.9348	0.0476	0.9063	0.0578	0.8395	0.0745	0.7621	0.0860
	0.100	0.9516	0.0382	0.9340	0.0456	0.8888	0.0606	0.8293	0.0747
	0.125	0.9624	0.0318	0.9495	0.0379	0.9148	0.0516	0.8657	0.0663
University of Pavia	0.050	0.9008	0.0438	0.8472	0.0558	0.7466	0.0711	0.6578	0.0783
	0.075	0.9434	0.0343	0.9189	0.0432	0.8640	0.0591	0.8020	0.0715
	0.100	0.9649	0.0275	0.9519	0.0340	0.9195	0.0477	0.8778	0.0607
	0.125	0.9778	0.0220	0.9700	0.0270	0.9496	0.0382	0.9201	0.0503
Washington, D.C	0.050	0.9010	0.0549	0.8536	0.0690	0.7649	0.0860	0.6840	0.0933
	0.075	0.9456	0.0417	0.9250	0.0514	0.8781	0.0689	0.8248	0.0835
	0.100	0.9674	0.0319	0.9566	0.0388	0.9301	0.0534	0.8954	0.0688
	0.125	0.9798	0.0245	0.9735	0.0297	0.9566	0.0417	0.9330	0.0560

proposed approach tends to be more confident of the result and is inferior to the coverage rate of with higher σ_0 . Higher σ_0 means the distribution is closer to the random impulse noise. Furthermore, since the solvers (either GoDec or ALM solver) are all based on SVD decomposition, our approach is of the same time complexity with the original LRMA methods.

IV. CONCLUSION

This is the first research to address the uncertainty quantification for LRMA based HSI denoising techniques. We provide a time-efficient closed-form uncertainty propagation model to quantify the element-wise uncertainty for the denoised HSI without any prior ground truth. We also propose a weighted average uncertainty formulation to tackle the ‘‘uncertainty mixing’’ problem caused by the sliding-window strategy in the large HSI denoising. Moreover, the proposed uncertainty estimation approach is independent of the choice of the LRMA solver. It is based on the global minimum assumption of LRMA, thus a more accurate algorithm leads to better performance of the uncertainty estimation. Extensive numerical experiments indicate that the proposed uncertainty quantification method is accurate and robust to describe the statistical behaviors of the estimations from the LRMA approach. The time consumption of the closed-form formulation is time-efficient to be deployed to any state-of-the-art LRMA algorithms. The uncertainty provided by our approach can be further applied to applications that require multi-source or multi-scale data fusion, data assimilation, and remote sensing product confidence estimation.

APPENDIX

Proof of Theorem 1. Suppose the selected LRMA solver achieves the optimal solution regarding the objective function Eq. (3), the optimizer $\hat{\mathbf{X}}, \hat{\mathbf{Y}}$ should satisfy the local minima of Eq. (3). Let’s denoted $F(\hat{\mathbf{X}}, \hat{\mathbf{Y}})$ as:

$$F(\hat{\mathbf{X}}, \hat{\mathbf{Y}}) = \frac{1}{2} \|\mathbf{W}^{(ijk)} - g^{-1}(\hat{\mathbf{X}}\hat{\mathbf{Y}}^\top)\|_{\mathbb{F}}^2 \quad (21)$$

$$\stackrel{(i)}{=} \frac{1}{2} \|\mathbf{W}^{\#(ijk)} - \hat{\mathbf{X}}\hat{\mathbf{Y}}^\top\|_{\mathbb{F}}^2,$$

where (i) is because $g^{-1}(\cdot)$ is the permutation function and $g(\mathbf{W}^{(ijk)}) = \mathbf{W}^{\#(ijk)}$. Assuming the solver yields $F(\hat{\mathbf{X}}, \hat{\mathbf{Y}})$ clos-

ing to the global minimum $F(\mathbf{X}^*, \mathbf{Y}^*)$. The first-order expansion of $F(\hat{\mathbf{X}}, \hat{\mathbf{Y}})$ is close to the zero matrix defined as \mathcal{O} . By following Eq. (1) and ignoring the random noise, we define the patch function:

$$\begin{aligned} \mathbf{W}^{(ijk)} &= \mathbf{W}^*(ijk) + \mathbf{G}^{(ijk)} \\ \mathbf{W}^{\#(ijk)} &= \mathbf{W}^{\#*}(ijk) + \mathbf{G}^{\#(ijk)}, \end{aligned} \quad (22)$$

where $\mathbf{G}^{\#(ijk)} = g(\mathbf{G}^{(ijk)})$. The optimizer $F(\hat{\mathbf{X}}, \hat{\mathbf{Y}})$ achieves local minima which is closing to the global minima, we then have the partial derivatives equal to zero matrix:

$$\begin{aligned} \frac{\partial F(\hat{\mathbf{X}}, \hat{\mathbf{Y}})}{\partial \hat{\mathbf{X}}} &\stackrel{(i)}{=} (\mathbf{W}^{\#(ijk)} - \hat{\mathbf{X}}\hat{\mathbf{Y}}^\top)\hat{\mathbf{Y}} \\ &= (\mathbf{G}^{\#(ijk)} + \mathbf{W}^*(ijk) - \hat{\mathbf{X}}\hat{\mathbf{Y}}^\top)\hat{\mathbf{Y}} \\ &= (\mathbf{G}^{\#(ijk)} + \mathbf{X}^*\mathbf{Y}^{*\top} - \hat{\mathbf{X}}\hat{\mathbf{Y}}^\top)\hat{\mathbf{Y}} \\ &\stackrel{(ii)}{\approx} (\mathbf{G}^{\#(ijk)} + \mathbf{X}^*\hat{\mathbf{R}}^\top\hat{\mathbf{Y}}^\top - \hat{\mathbf{X}}\hat{\mathbf{Y}}^\top)\hat{\mathbf{Y}} \approx \mathcal{O}, \end{aligned} \quad (23)$$

$$\begin{aligned} \frac{\partial F(\hat{\mathbf{X}}, \hat{\mathbf{Y}})}{\partial \hat{\mathbf{Y}}} &\stackrel{(i)}{=} \hat{\mathbf{X}}^\top(\mathbf{W}^{\#(ijk)} - \hat{\mathbf{X}}\hat{\mathbf{Y}}^\top) \\ &= \hat{\mathbf{X}}^\top(\mathbf{G}^{\#(ijk)} + \mathbf{W}^*(ijk) - \hat{\mathbf{X}}\hat{\mathbf{Y}}^\top) \\ &= \hat{\mathbf{X}}^\top(\mathbf{G}^{\#(ijk)} + \mathbf{X}^*\mathbf{Y}^{*\top} - \hat{\mathbf{X}}\hat{\mathbf{Y}}^\top) \\ &\stackrel{(ii)}{\approx} \hat{\mathbf{X}}^\top(\mathbf{G}^{\#(ijk)} + \hat{\mathbf{X}}\hat{\mathbf{R}}\mathbf{Y}^{*\top} - \hat{\mathbf{X}}\hat{\mathbf{Y}}^\top) \approx \mathcal{O}, \end{aligned} \quad (24)$$

where (i) is resulted from $d\mathbf{W}^{\#(ijk)} = d\hat{\mathbf{X}}\hat{\mathbf{Y}}^\top + \hat{\mathbf{X}}(d\hat{\mathbf{Y}})^\top$. (ii) is approximated by the fact that the rectified local minima $(\hat{\mathbf{X}}\hat{\mathbf{R}}, \hat{\mathbf{Y}}\hat{\mathbf{R}})$ are close to global minima $(\mathbf{X}^*, \mathbf{Y}^*)$. We manipulate Eq. (23) and Eq. (24) to:

$$\begin{aligned} \mathbf{G}^{\#(ijk)}\hat{\mathbf{Y}} &\approx (\hat{\mathbf{X}} - \mathbf{X}^*\hat{\mathbf{R}}^\top)\hat{\mathbf{Y}}^\top\hat{\mathbf{Y}} \\ (\hat{\mathbf{X}} - \mathbf{X}^*\hat{\mathbf{R}}^\top) &\approx \mathbf{G}^{\#(ijk)}\hat{\mathbf{Y}}(\hat{\mathbf{Y}}^\top\hat{\mathbf{Y}})^{-1} \\ (\hat{\mathbf{X}}\hat{\mathbf{R}} - \mathbf{X}^*) &\approx \mathbf{G}^{\#(ijk)}\hat{\mathbf{Y}}(\hat{\mathbf{Y}}^\top\hat{\mathbf{R}}^\top\hat{\mathbf{R}}\hat{\mathbf{Y}})^{-1}\hat{\mathbf{R}} \\ (\hat{\mathbf{X}}\hat{\mathbf{R}} - \mathbf{X}^*) &\stackrel{(i)}{\approx} \mathbf{G}^{\#(ijk)}\hat{\mathbf{Y}}\hat{\mathbf{R}}(\hat{\mathbf{Y}}^\top\hat{\mathbf{R}}^\top\hat{\mathbf{R}}\hat{\mathbf{Y}})^{-1} \\ (\hat{\mathbf{R}}^\top\hat{\mathbf{X}}^\top - \mathbf{X}^{*\top})\mathbf{e}_v &\approx [\mathbf{G}^{\#(ijk)}\hat{\mathbf{Y}}(\hat{\mathbf{Y}}^\top\hat{\mathbf{Y}})^{-1}]^\top\mathbf{e}_v \stackrel{(ii)}{\approx} \mathcal{N}(0, \sigma_0^2(\Sigma^*)^{-1}), \end{aligned} \quad (25)$$

$$\begin{aligned}
\hat{\mathbf{X}}^T \mathbf{G}^{\#(ijk)} &= \hat{\mathbf{X}}^T \hat{\mathbf{X}} (\hat{\mathbf{Y}}^T - \hat{\mathbf{R}} \mathbf{Y}^* \mathbf{T}) \\
(\hat{\mathbf{Y}}^T - \hat{\mathbf{R}} \mathbf{Y}^* \mathbf{T}) &\approx (\hat{\mathbf{X}}^T \hat{\mathbf{X}})^{-1} \hat{\mathbf{X}}^T \mathbf{G}^{\#(ijk)} \\
(\hat{\mathbf{R}}^T \hat{\mathbf{Y}}^T - \mathbf{Y}^* \mathbf{T}) &\approx \hat{\mathbf{R}}^T (\hat{\mathbf{X}}^T \hat{\mathbf{R}}^T \hat{\mathbf{R}} \hat{\mathbf{X}})^{-1} \hat{\mathbf{X}}^T \mathbf{G}^{\#(ijk)} \\
(\hat{\mathbf{R}}^T \hat{\mathbf{Y}}^T - \mathbf{Y}^* \mathbf{T}) &\stackrel{(i)}{\approx} (\hat{\mathbf{X}}^T \hat{\mathbf{R}}^T \hat{\mathbf{R}} \hat{\mathbf{X}})^{-1} \hat{\mathbf{R}}^T \hat{\mathbf{X}}^T \mathbf{G}^{\#(ijk)} \\
(\hat{\mathbf{R}}^T \hat{\mathbf{Y}}^T - \mathbf{Y}^* \mathbf{T}) \mathbf{e}_v &\approx (\hat{\mathbf{X}}^T \hat{\mathbf{X}})^{-1} \hat{\mathbf{X}}^T \mathbf{G}^{\#(ijk)} \mathbf{e}_v \stackrel{(iii)}{\sim} \mathcal{N}(0, \sigma_0^2 (\Sigma^*)^{-1}),
\end{aligned} \tag{26}$$

where the matrix exchange in step (i) is enabled by the fact that $(\hat{\mathbf{X}}^T \hat{\mathbf{R}}^T \hat{\mathbf{R}} \hat{\mathbf{X}})$ and $(\hat{\mathbf{Y}}^T \hat{\mathbf{R}}^T \hat{\mathbf{R}} \hat{\mathbf{Y}})$ are diagonal matrix. We denote the rectified local minima $(\hat{\mathbf{X}}, \hat{\mathbf{Y}})$ equal to $(\hat{\mathbf{X}} \hat{\mathbf{R}}, \hat{\mathbf{Y}} \hat{\mathbf{R}})$ for the benefit of concise presentation.

The prove of step (ii): Each element of the Gaussian noise matrix $\mathbf{G}^{\#(ijk)} \sim \mathcal{N}(0, \sigma^2)$. According to Eq. (7), Σ^* is a diagonal matrix and the diagonal element at position $[i, i]$ $(\Sigma_{ii}^*)^{-1}$ equals to $1/\|\mathbf{X}_{:,i}\|_2^2$ or $1/\|\mathbf{Y}_{:,i}\|_2^2$ where $\hat{\mathbf{X}}_{:,i}$ or $\hat{\mathbf{Y}}_{:,i}$ is the i th column of matrix $\hat{\mathbf{X}}$ or $\hat{\mathbf{Y}}$.

The proof of (i):

$$\begin{aligned}
&[\mathbf{G}^{\#(ijk)} \hat{\mathbf{Y}} (\hat{\mathbf{Y}}^T \hat{\mathbf{Y}})^{-1}]^T \mathbf{e}_v \\
&= \left[\sum_{i=1}^L \frac{1}{\|\hat{\mathbf{Y}}_{:,i}\|_2^2} \hat{\mathbf{Y}}_{i1} \mathbf{G}_{vi}^{\#(ijk)} \dots \sum_{i=1}^L \frac{1}{\|\hat{\mathbf{Y}}_{:,r}\|_2^2} \hat{\mathbf{Y}}_{ir} \mathbf{G}_{vi}^{\#(ijk)} \right].
\end{aligned} \tag{27}$$

Take the first element $\sum_{i=1}^L \frac{1}{\|\hat{\mathbf{Y}}_{:,i}\|_2^2} \hat{\mathbf{Y}}_{i1} \mathbf{G}_{vi}^{\#(ijk)}$ as an example:

$$\begin{aligned}
\text{var} \left(\sum_{i=1}^L \frac{1}{\|\hat{\mathbf{Y}}_{:,i}\|_2^2} \hat{\mathbf{Y}}_{i1} \mathbf{G}_{vi}^{\#(ijk)} \right) &= \left(\sum_{i=1}^L \frac{1}{\|\hat{\mathbf{Y}}_{:,i}\|_2^2} \hat{\mathbf{Y}}_{i1} \right)^2 \sigma_0^2 \\
&= \frac{1}{(\|\hat{\mathbf{Y}}_{:,1}\|_2^2)^2} \left(\sum_{i=1}^L \hat{\mathbf{Y}}_{i1} \right)^2 \sigma_0^2 \\
&= \frac{1}{(\|\hat{\mathbf{Y}}_{:,1}\|_2^2)} \sigma_0^2 \\
&\approx (\Sigma_{11}^*)^{-1} \sigma_0^2.
\end{aligned} \tag{28}$$

The same conclusion also applies to other elements. Similarly, the proof of (ii):

$$\begin{aligned}
&(\hat{\mathbf{X}}^T \hat{\mathbf{X}})^{-1} \hat{\mathbf{X}} \mathbf{G}^{\#(ijk)} \mathbf{e}_v \\
&= \left[\sum_{i=1}^K \frac{1}{\|\hat{\mathbf{X}}_{:,i}\|_2^2} \hat{\mathbf{X}}_{i1} \mathbf{G}_{iv}^{\#(ijk)} \dots \sum_{i=1}^K \frac{1}{\|\hat{\mathbf{X}}_{:,r}\|_2^2} \hat{\mathbf{X}}_{ir} \mathbf{G}_{iv}^{\#(ijk)} \right]
\end{aligned} \tag{29}$$

Take the first element $\sum_{i=1}^K \frac{1}{\|\hat{\mathbf{X}}_{:,i}\|_2^2} \hat{\mathbf{X}}_{i1} \mathbf{G}_{iv}^{\#(ijk)}$ as an example:

$$\begin{aligned}
\text{var} \left(\sum_{i=1}^K \frac{1}{\|\hat{\mathbf{X}}_{:,i}\|_2^2} \hat{\mathbf{X}}_{i1} \mathbf{G}_{iv}^{\#(ijk)} \right) &= \left(\sum_{i=1}^K \frac{1}{\|\hat{\mathbf{X}}_{:,i}\|_2^2} \hat{\mathbf{X}}_{i1} \right)^2 \sigma_0^2 \\
&= \frac{1}{(\|\hat{\mathbf{X}}_{:,1}\|_2^2)^2} \left(\sum_{i=1}^K \hat{\mathbf{X}}_{i1} \right)^2 \sigma_0^2 \\
&= \frac{1}{(\|\hat{\mathbf{X}}_{:,1}\|_2^2)} \sigma_0^2 \\
&\approx (\Sigma_{11}^*)^{-1} \sigma_0^2.
\end{aligned} \tag{30}$$

The same conclusion also applies to other elements.

This concludes the proof of (i) and (ii) and also the proof of **theorem 1**.

REFERENCES

- [1] H. Dehghan and H. Ghassemian, "Measurement of uncertainty by the entropy: application to the classification of mss data," *International journal of remote sensing*, vol. 27, no. 18, pp. 4005–4014, 2006.
- [2] G. M. Foody and P. M. Atkinson, *Uncertainty in remote sensing and GIS*. John Wiley & Sons, 2003.
- [3] W. Verhoef and H. Bach, "Coupled soil–leaf–canopy and atmosphere radiative transfer modeling to simulate hyperspectral multi-angular surface reflectance and toa radiance data," *Remote Sensing of Environment*, vol. 109, no. 2, pp. 166–182, 2007.
- [4] X. Chen, K. Yu, and H. Wu, "Determination of minimum detectable deformation of terrestrial laser scanning based on error entropy model," *IEEE Transactions on Geoscience and Remote Sensing*, vol. 56, no. 1, pp. 105–116, 2017.
- [5] X. Du and A. Zare, "Multiresolution multimodal sensor fusion for remote sensing data with label uncertainty," *IEEE Transactions on Geoscience and Remote Sensing*, 2019.
- [6] R. Senge, S. Bösner, K. Dembczyński, J. Haasenritter, O. Hirsch, N. Donner-Banzhoff, and E. Hüllermeier, "Reliable classification: Learning classifiers that distinguish aleatoric and epistemic uncertainty," *Information Sciences*, vol. 255, pp. 16–29, 2014.
- [7] A. Oxley, *Uncertainties in GPS Positioning: A mathematical discourse*. Academic Press, 2017.
- [8] L. Bastin, P. F. Fisher, and J. Wood, "Visualizing uncertainty in multi-spectral remotely sensed imagery," *Computers & Geosciences*, vol. 28, no. 3, pp. 337–350, 2002.
- [9] E. Sarhrouni, A. Hammouch, and D. Aboutajdine, "Application of symmetric uncertainty and mutual information to dimensionality reduction and classification of hyperspectral images," *arXiv preprint arXiv:1211.0613*, 2012.
- [10] Y. Zhou, A. Rangarajan, and P. D. Gader, "A spatial compositional model for linear unmixing and endmember uncertainty estimation," *IEEE Transactions on Image Processing*, vol. 25, no. 12, pp. 5987–6002, 2016.
- [11] M.-E. Polo, Á. M. Felicísimo, A. G. Villanueva, and J.-Á. Martínez-del Pozo, "Estimating the uncertainty of terrestrial laser scanner measurements," *IEEE transactions on geoscience and remote sensing*, vol. 50, no. 11, pp. 4804–4808, 2012.
- [12] P. Ghamisi, N. Yokoya, J. Li, W. Liao, S. Liu, J. Plaza, B. Rasti, and A. Plaza, "Advances in hyperspectral image and signal processing: A comprehensive overview of the state of the art," *IEEE Geoscience and Remote Sensing Magazine*, vol. 5, no. 4, pp. 37–78, 2017.
- [13] Q. Zhang, Q. Yuan, J. Li, X. Liu, H. Shen, and L. Zhang, "Hybrid noise removal in hyperspectral imagery with a spatial–spectral gradient network," *IEEE Transactions on Geoscience and Remote Sensing*, vol. 57, no. 10, pp. 7317–7329, 2019.
- [14] A. Buades, B. Coll, and J.-M. Morel, "A non-local algorithm for image denoising," in *2005 IEEE Computer Society Conference on Computer Vision and Pattern Recognition (CVPR'05)*, vol. 2. IEEE, 2005, pp. 60–65.
- [15] M. Maggioni, V. Katkovnik, K. Egiazarian, and A. Foi, "Nonlocal transform-domain filter for volumetric data denoising and reconstruction," *IEEE transactions on image processing*, vol. 22, no. 1, pp. 119–133, 2012.
- [16] Y. Qian and M. Ye, "Hyperspectral imagery restoration using nonlocal spectral-spatial structured sparse representation with noise estimation," *IEEE Journal of Selected Topics in Applied Earth Observations and Remote Sensing*, vol. 6, no. 2, pp. 499–515, 2012.
- [17] K. Dabov, A. Foi, V. Katkovnik, and K. Egiazarian, "Image denoising by sparse 3-d transform-domain collaborative filtering," *IEEE Transactions on image processing*, vol. 16, no. 8, pp. 2080–2095, 2007.
- [18] Q. Yuan, L. Zhang, and H. Shen, "Hyperspectral image denoising employing a spectral–spatial adaptive total variation model," *IEEE Transactions on Geoscience and Remote Sensing*, vol. 50, no. 10, pp. 3660–3677, 2012.
- [19] J. Li, Q. Yuan, H. Shen, and L. Zhang, "Noise removal from hyperspectral image with joint spectral–spatial distributed sparse representation," *IEEE Transactions on Geoscience and Remote Sensing*, vol. 54, no. 9, pp. 5425–5439, 2016.
- [20] H. Zhang, W. He, L. Zhang, H. Shen, and Q. Yuan, "Hyperspectral image restoration using low-rank matrix recovery," *IEEE Transactions on Geoscience and Remote Sensing*, vol. 52, no. 8, pp. 4729–4743, 2013.
- [21] L. Zhuang and J. M. Bioucas-Dias, "Fast hyperspectral image denoising and inpainting based on low-rank and sparse representations," *IEEE Journal of Selected Topics in Applied Earth Observations and Remote Sensing*, vol. 11, no. 3, pp. 730–742, 2018.

- [22] W. He, H. Zhang, L. Zhang, and H. Shen, "Hyperspectral image denoising via noise-adjusted iterative low-rank matrix approximation," *IEEE Journal of Selected Topics in Applied Earth Observations and Remote Sensing*, vol. 8, no. 6, pp. 3050–3061, 2015.
- [23] Q. Yuan, Q. Zhang, J. Li, H. Shen, and L. Zhang, "Hyperspectral image denoising employing a spatial-spectral deep residual convolutional neural network," *IEEE Transactions on Geoscience and Remote Sensing*, vol. 57, no. 2, pp. 1205–1218, 2018.
- [24] W. He, H. Zhang, L. Zhang, and H. Shen, "Total-variation-regularized low-rank matrix factorization for hyperspectral image restoration," *IEEE transactions on geoscience and remote sensing*, vol. 54, no. 1, pp. 178–188, 2015.
- [25] J. M. Bioucas-Dias and J. M. Nascimento, "Hyperspectral subspace identification," *IEEE Transactions on Geoscience and Remote Sensing*, vol. 46, no. 8, pp. 2435–2445, 2008.
- [26] Y. Chen, X. Cao, Q. Zhao, D. Meng, and Z. Xu, "Denoising hyperspectral image with non-iid noise structure," *IEEE transactions on cybernetics*, vol. 48, no. 3, pp. 1054–1066, 2017.
- [27] H. Fan, C. Li, Y. Guo, G. Kuang, and J. Ma, "Spatial-spectral total variation regularized low-rank tensor decomposition for hyperspectral image denoising," *IEEE Transactions on Geoscience and Remote Sensing*, vol. 56, no. 10, pp. 6196–6213, 2018.
- [28] Y. Chen, W. He, N. Yokoya, and T.-Z. Huang, "Hyperspectral image restoration using weighted group sparsity-regularized low-rank tensor decomposition," *IEEE transactions on cybernetics*, 2019.
- [29] B. Aiazzi, L. Alparone, A. Barducci, S. Baronti, P. Marcoionni, I. Pippi, and M. Selva, "Noise modelling and estimation of hyperspectral data from airborne imaging spectrometers," *Annals of Geophysics*, vol. 49, no. 1, 2006.
- [30] N. Acito, M. Diani, and G. Corsini, "Signal-dependent noise modeling and model parameter estimation in hyperspectral images," *IEEE Transactions on Geoscience and Remote Sensing*, vol. 49, no. 8, pp. 2957–2971, 2011.
- [31] Y. Chen, J. Fan, C. Ma, and Y. Yan, "Inference and uncertainty quantification for noisy matrix completion," *arXiv preprint arXiv:1906.04159*, 2019.
- [32] Y. Chen, Y. Chi, J. Fan, C. Ma, and Y. Yan, "Noisy matrix completion: Understanding statistical guarantees for convex relaxation via nonconvex optimization," *arXiv preprint arXiv:1902.07698*, 2019.
- [33] J. Wright, A. Ganesh, S. Rao, Y. Peng, and Y. Ma, "Robust principal component analysis: Exact recovery of corrupted low-rank matrices via convex optimization," in *Advances in neural information processing systems*, 2009, pp. 2080–2088.
- [34] T. Zhou and D. Tao, "Godec: Randomized low-rank & sparse matrix decomposition in noisy case," in *Proceedings of the 28th International Conference on Machine Learning, ICML 2011*, 2011.
- [35] G. Casella and R. L. Berger, *Statistical inference*. Duxbury Pacific Grove, CA, 2002, vol. 2.
- [36] R. M. Gray, *Entropy and information theory*. Springer Science & Business Media, 2011.
- [37] G. Vane, R. O. Green, T. G. Chrien, H. T. Enmark, E. G. Hansen, and W. M. Porter, "The airborne visible/infrared imaging spectrometer (aviris)," *Remote sensing of environment*, vol. 44, no. 2-3, pp. 127–143, 1993.
- [38] R. O. Green, M. L. Eastwood, C. M. Sarture, T. G. Chrien, M. Aronsson, B. J. Chippendale, J. A. Faust, B. E. Pavri, C. J. Chovit, M. Solis *et al.*, "Imaging spectroscopy and the airborne visible/infrared imaging spectrometer (aviris)," *Remote sensing of environment*, vol. 65, no. 3, pp. 227–248, 1998.